






Aerodynamic performance of a free-flying dragonfly—A span-resolved investigation

Cite as: Phys. Fluids **32**, 041903 (2020); <https://doi.org/10.1063/1.5145199>

Submitted: 16 January 2020 . Accepted: 21 March 2020 . Published Online: 15 April 2020

C. Hefler , R. Noda , H. H. Qiu , and W. Shyy 

COLLECTIONS

 This paper was selected as Featured



View Online



Export Citation



CrossMark

ARTICLES YOU MAY BE INTERESTED IN

[Flow separation around a square cylinder at low to moderate Reynolds numbers](#)

Physics of Fluids **32**, 044103 (2020); <https://doi.org/10.1063/5.0005757>

[Effects of the intrinsic curvature of elastic filaments on the propulsion of a flagellated microrobot](#)

Physics of Fluids **32**, 041902 (2020); <https://doi.org/10.1063/1.5143372>

[Vortex shedding characteristics in the wake of circular finned cylinders](#)

Physics of Fluids **32**, 045113 (2020); <https://doi.org/10.1063/5.0005079>



NEW: TOPIC ALERTS

Explore the latest discoveries in your field of research

SIGN UP TODAY!





Aerodynamic performance of a free-flying dragonfly—A span-resolved investigation

Cite as: Phys. Fluids 32, 041903 (2020); doi: 10.1063/1.5145199

Submitted: 16 January 2020 • Accepted: 21 March 2020 •

Published Online: 15 April 2020



C. Hefler,¹  R. Noda,²  H. H. Qiu,^{1,a)}  and W. Shyy¹ 

AFFILIATIONS

¹Department of Mechanical and Aerospace Engineering, The Hong Kong University of Science and Technology, Clear Water Bay, Kowloon, Hong Kong

²Department of Aeronautics and Astronautics, Kyoto University, Nishikyo, Kyoto 615-8540, Japan

^{a)}Author to whom correspondence should be addressed: meqiu@ust.hk. Tel.: (+852) 2358 7190. Fax: (+852) 2358 1543

ABSTRACT

We present a quantitative characterization of the unsteady aerodynamic features of a live, free-flying dragonfly under a well-established flight condition. In particular, our investigations cover the span-wise features of vortex interactions between the fore- and hind-pairs of wings that could be a distinctive feature of a high aspect ratio tandem flapping wing pair. Flapping kinematics and dynamic wing-shape deformation of a dragonfly were measured by tracking painted landmarks on the wings. Using it as the input, computational fluid dynamics analyses were conducted, complemented with time-resolved particle image velocimetry flow measurements to better understand the aerodynamics associated with a dragonfly. The results show that the flow structures around hindwing's inner region are influenced by forewing's leading edge vortex, while those around hindwing's outer region are more influenced by forewing's shed trailing edge vortex. Using a span-resolved approach, we found that the forewing–hindwing interactions affect the horizontal force (thrust) generation of the hindwing most prominently and the modulation of the force generation is distributed evenly around the midspan. Compared to operating in isolation, the thrust of the hindwing is largely increased during upstroke, albeit the drag is also slightly increased during the downstroke. The vertical force generation is moderately affected by the forewing–hindwing interactions and the modulation takes place in the outer 40% of the hindwing span during the downstroke and in the inner 60% of the span during the upstroke.

Published under license by AIP Publishing. <https://doi.org/10.1063/1.5145199>

I. INTRODUCTION

Dragonflies are remarkable flyers and offer excellent insight into the aerodynamics and fluid–structural interactions as well as the various inter-wing interactions between tandem-coupled flexible flapping wings.^{1,2} Flapping wing locomotion is technically relevant in the field of micro air vehicles (MAVs) and considered to be most feasible for indoor missions.³

Observations on free-flying and tethered dragonflies suggest that in-phase flapping is used to generate high aerodynamic forces for demanding quick maneuvers or take off, while out-of-phase flapping is favored for steady flight and hovering.^{4–6} Little or moderate changes in the flapping pattern of the dragonfly can cause substantial changes in the aerodynamic forces generated.^{7,8} It is hypothesized that dragonflies smartly profit from the interaction between their wings, and it is of active interest how such unsteady effects could be

exploited to advance the performance of biomimetic flapping wing MAVs.^{9–11}

Interaction effects between tandem-coupled wings can generally fall into two categories: induced flow effects (downwash or upwash flow) and direct vortex interactions. Numerical^{12–14} and experimental^{15–20} studies of hovering flight mode with both horizontal^{16,18,19} and inclined^{12–15,17,20} stroke planes have found the downwash effect to be detrimental to vertical force generation. Nevertheless, by optimal phasing of the wings, the downwash effect is reduced and wings can generate forces nearly equal^{12,14–17,19} or higher²⁰ than wings that operate in isolation; Hu and Deng²⁰ proposed that the common observation^{4–6,21,22} that hovering dragonflies use out-of-phase flapping is reasonable as it comes with only about 10% lift reduction (in comparison with the highest lift of in-phase flapping), but there is improved flight stability because of reduced body oscillations. It is found that hovering with four wings needs 22% less power

than hovering with two wings.¹⁸ Additionally, Wang and Russell¹⁴ concluded that a relatively wide range of wing phasing (100° – 220° hind-wing lead) can generate the required vertical force for steady hovering, with good power efficiency.

One of the key attributes of how a flapping wing generates lift is the delayed stall of the leading edge vortex (LEV) that can result in substantial aerodynamic force to a flapping wing system.^{23–25} As much as 80% increase in lift can be attributed to the LEV in case of impulsively started model wings at an angle of attack above 13.5° .²³ Fundamentally, the LEV is generated and sustained from the balance between the pressure gradient, the centripetal force, and the Coriolis force in the Navier–Stokes equations. The LEV generates a lower pressure area in its core, which results in an increased suction force on the wing surface. The effect of LEV and its stability has been studied extensively in recent years.^{26–28} Direct vortex interactions could intensify or attenuate LEV formation and affect its shedding. Several studies aimed to characterize direct vortex interactions between tandem-coupled wings.

Fusion with the forewing shed trailing edge vortex (TEV) can enhance or diminish the LEV of the hindwing.¹⁶ Vortex entities forming close to each other (usually the case when the wings are flapping in-phase) can synergistically boost each other.^{20,29} Induced flow of a shed forewing vortex can also affect the effective angle of the attack of the hindwing.¹⁹

Vortex interactions^{30–34} and downwash^{35,36} were linked to changes in aerodynamic performance at different phasings in forward flight mode as well. It is concluded by these works that the larger the advance ratio (non-dimensional flight speed), the sooner the forewing wake elements may interact with the hindwing.

In summary, a number of scenarios can affect the performance of a tandem winged flight system, including global boundary conditions (such as an incoming flow or wall effect), flapping kinematic parameters (phasing of the wings most importantly), and wings' geometrical setup and structural properties. While past studies considerably have helped our understanding of tandem wing aerodynamics, the consequences of inter-wing interactions were often only evaluated on a systems level. Previous investigations paid little attention to how interaction features vary over the span of a high aspect ratio root flapping system such as that of a dragonfly. Moreover, using simplified parameter space and wing models result in aerodynamic features that differ from those of a real dragonfly.³⁷ On the other hand, full span qualitative and quantitative studies involving live dragonflies are attempted only by a few.^{37–39}

Tethered and free-flying dragonflies were studied qualitatively using smoke visualization by Thomas *et al.*³⁸ It was hypothesized that the forewing LEV spans over the dragonfly body from tip to tip, while the hindwing typically exhibits attached flow. Interaction effects in the wake have been presented, but interaction effects in the proximity of the wings could not be clearly observed.³⁸ Some of the findings were quantitatively confirmed for out-of-phase flapping by repeating the experiment with *Aeshna* and *Sympetrum* specimens, measuring the flow with stereo time-resolved particle image velocimetry (TR-PIV).³⁹ In this study, they found that spanwise contribution to weight support increases from root to tip, and both species are approximately able to support their weight solely by the contribution of the forewing LEV.³⁹

Most recently, Hefler *et al.* presented interaction scenarios along the wingspan of a live tethered dragonfly.³⁷ The effect of the

interaction between separate vortex entities in the inner region of the hindwing was evaluated based on the circulation boost of the hindwing LEV. It was also established that a free-flying dragonfly in the low speed forward flight regime could exhibit similar flow features as a tethered specimen.³⁷

Based on our previous investigation, this work is aimed to characterize the interaction features in detail and the resulting aerodynamic force distribution resolved to the wingspan of a free-flying dragonfly, decoupled from the imposed effect of an external flow. For the current study, we use not only the previously established experimental methodology but an accurate computational fluid dynamics (CFD) simulation as well. We believe that understanding the characteristic spanwise functionality exhibited under the instinctive control of the dragonfly can be the basis of the development and optimization of a novel bioinspired wing. Advanced nanofabrication could allow a flexible wing to better utilize the dominant inter-wing interactions by smart effective stiffness distribution that provides an optimized passive shape deformation.

II. MATERIALS AND METHODS

A. Experimental free-flight flow and dynamic wing-shape measurement

Pantala flavescens (Fabricius 1798) individuals [Fig. 1(a)] were caught near the Hong Kong University of Science and Technology campus. It is a medium sized dragonfly with a tip-to-tip wingspan of 80–90 mm and body length of about 50 mm. The dragonflies were used within a few hours of capture, allowing sufficient time for the specimen to adapt to the temperature (19°C) in the laboratory. Seven specimens were used for free-flight flow and two specimens for wing-shape measurements. Each specimen could be used for a limited number of flights before getting overly exhausted. In the PIV measurements, the light sheet crossing the spanwise position of a free-flight dragonfly is difficult to control, which often resulted in an invalid measurement. This made it necessary to use more specimens for PIV measurement than were used for the wing-shape measurements. To illustrate the representative flow features and measure the dynamic wing-shape deformation of a free-flying dragonfly, we used the flights when the specimen flew steadily following a relatively straight path in the measurement region.

A flight chamber [Fig. 1(b)] of 2 m (W) \times 2 m (L) \times 2 m (H) was built indoors, with black curtain walls having openings that allowed for direct accessibility to the high-speed cameras, the laser light, and the guiding light. Inside the flight chamber, there was no substantial flow present while the experiments were conducted. A strong incandescent studio lamp was used as the guiding light for the measurements. The dragonflies were first hand-held, then smoothly released inside the flight chamber, and flew typically toward the guiding light. The point of release was about a meter distant from the area where the measurement took place; it ensured that the dragonfly had a balanced natural flight when measured. A dark background was set for the PIV experiments, and a whiteboard background was used for capture of the wing motion and deformation.

The flow fields around the flapping wings of free-flying dragonflies were measured by stereo TR-PIV. A vertically aligned laser light sheet of about 1 mm thickness at the measurement field of view was used to illuminate the seeding particles [a mist of olive oil from

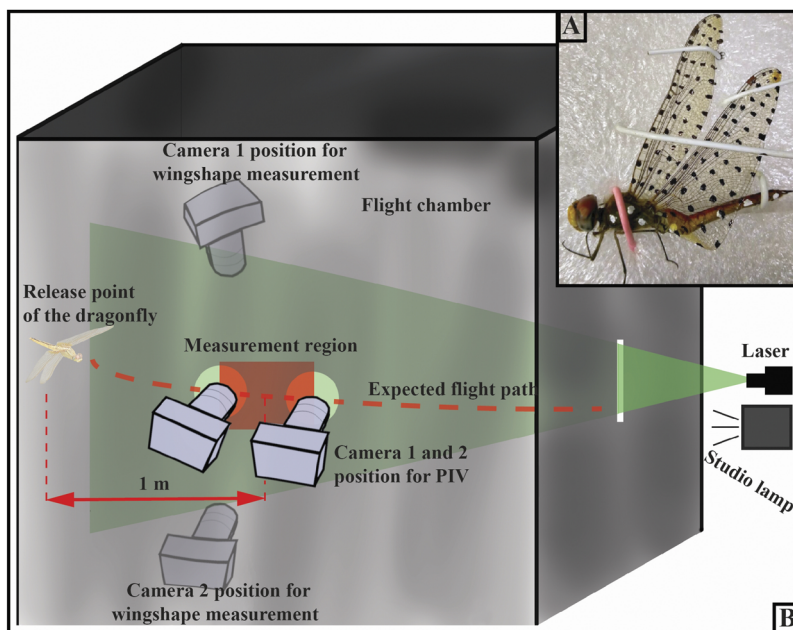


FIG. 1. Experimental procedures. (a) The dragonfly, *Pantala flavescens*, with markings on the wings. (b) The experimental layout for the free-flight measurements.

a compressed air aerosol generator [LaVision GmbH]). Flow field areas of approximately $130 \times 70 \text{ mm}^2$ were recorded using two high-speed CMOS-sensor cameras in double frame mode (VC-Phantom M310). The measurement was set to 1000 Hz with adequate frame separation interval within the range of 150–200 μs . The spanwise positions of the measurements could not be pre-set as the dragonfly was flying freely, quasi-parallel with the plane of the laser light sheet. From the recorded flights, we selected measurements to present three spanwise regions, in particular, the inner span, the midspan, and the outer span. The recorded frames were filtered to correct for intensity fluctuations. There is strong light reflection from the wing surface which has to be masked out to avoid affecting the calculated vector field. To obtain a clear result of the vector field, we applied direct masking on a case by case basis if pre-implemented masking functions were ineffective. Vector fields were computed using stereo cross correlation mode and stepwise decreasing interrogation window size to 32×32 pixels in the final pass. Vectors were validated by correlation peak criteria before a median filtering was applied to remove outliers. The final vector fields were smoothed. The error in PIV comes from the loss of particle image pairs due to the out of plane particle motion or bias error (ϵ_{bias}), the particle image diameter (ϵ_{rms0}), particle image displacement ($\epsilon_{\text{rms}\delta}$), interrogation window particle density (ϵ_{rmsp}), and the variations in particle image intensities (ϵ_{rmsi}).⁴⁰ To estimate the error, we follow the methods of Raffel *et al.*⁴⁰ In our measurements, the errors are $\epsilon_{\text{bias}} = 0.07$, $\epsilon_{\text{rms0}} = 0.007$, $\epsilon_{\text{rms}\delta} = 0.003$, $\epsilon_{\text{rmsp}} = 0.004$, $\epsilon_{\text{rmsi}} = 0.01$ (after intensity normalization in the image pre-processing). The total error is $\Sigma \epsilon_{\text{PIV}} = 0.094$ pixel or about 0.07 m/s (that is typically below 3%–5% of the measured velocity magnitudes in the wake and surroundings of the wings of the free-flying dragonfly).

Dynamic wing-shape deformation of four flights was recorded where the markers on the wings could be well identified for at

least two flapping cycles (the kinematic parameters of the recorded flights are presented in Fig. 2). Among the measured flights, one was selected for the numerical simulation after careful consideration of flight path and speed, flapping kinematics, and body posture to be representative of a typical slow forward flight mode of the species. In this case, the specimen was flying in a similar manner as in the case of the free-flight flow measurements: ascending flight with moderate speed, with about a quarter cycle hindwing lead wing phasing. To precisely measure the wing kinematics and the dynamic shape deformation of the wing membrane of the free-flying dragonfly, several dozen landmarks were painted on the fore- and hind-wing surfaces and on the body [Fig. 1(a)]. The dragonfly was filmed using two high-speed cameras (VC-Phantom M310) with the resolution of 1216×760 pixels. The cameras were placed above and below the flight path to ensure good visibility of the markers [Fig. 1(b)]. Considering the flapping frequency and size of the dragonfly, the cameras were synchronized at 2000 frames per second. The landmarks were tracked manually in each frame, and three-dimensional coordinates were reconstructed with a direct linear transformation (DLT) method via the open-source MATLAB-based application, DLTdv5.⁴¹ The application was used for this work without any alteration of its source code. The DLT coefficients were acquired with the help of a $190 \times 94 \times 118 \text{ mm}^3$ sized calibration frame. 33 and 37 markers were tracked on the hindwing and the forewing, respectively, which offered the most detailed DLT shape reconstruction of dragonfly wings to date. The careful manual tracking ensured that the positional uncertainty was at most one pixel (0.33 mm). All reconstructed points on the wing surfaces and body were smoothed by a fourth-order, low-pass Butterworth filter with a feasible cutoff frequency which was set to be lower than the Nyquist frequency but higher than the flapping frequency. The filtering ensured the removal of all high frequency errors due to the manual tracking

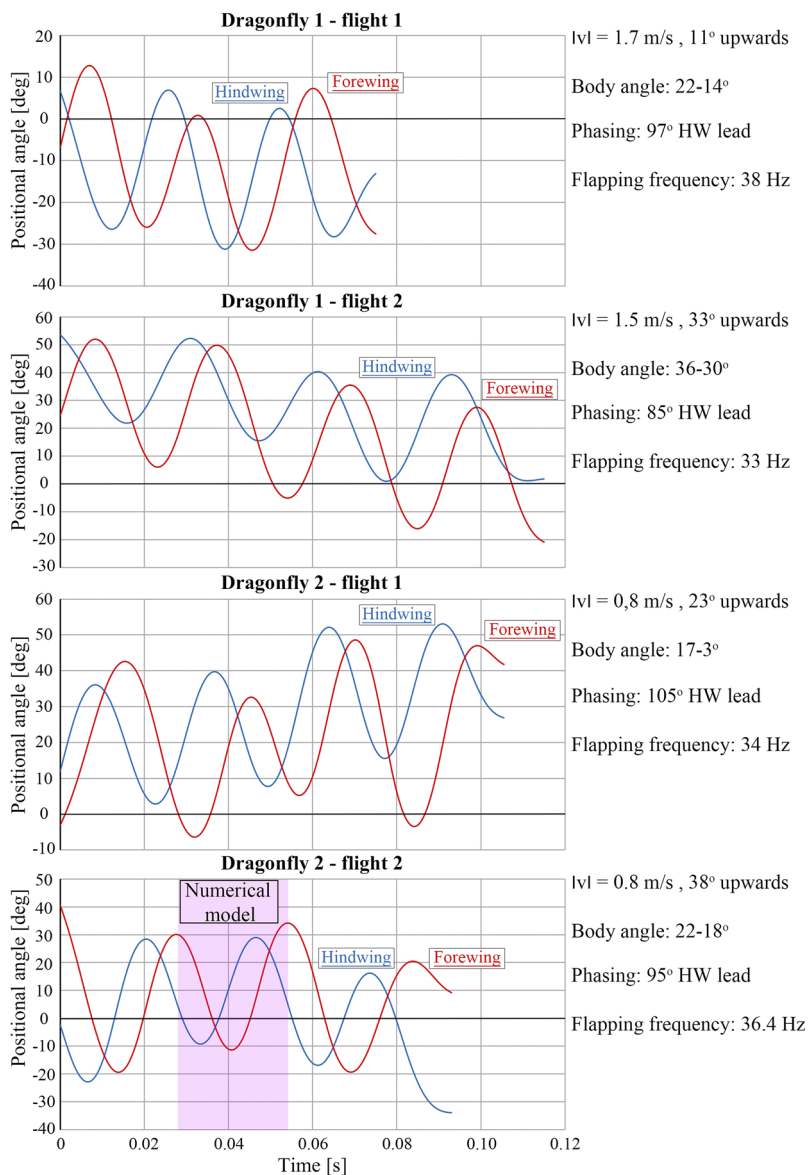


FIG. 2. Kinematics of the observed flights during the wing-shape deformation measurement. The body angle is given with its maximum and minimum observed values; $|v|$ is the average flight speed with notation of the average flight direction of the dragonfly.

process. The acquired coordinates are transformed to the computational domain of the numerical model.

B. Numerical model

The computational domain, the body orientation, and the flapping wing kinematics are described with the help of the global (X - Y - Z , with its origin at the corner of the computational domain), the wing-fixed (x' - y' - z' , with their origin at the root of each wing) and the body-fixed (x_b - y_b - z_b , with its origin in the center of mass of the dragonfly model) coordinate systems [Fig. 3(a)]. The transformations among these three coordinate systems are easy to establish to facilitate the dynamic regridding of the computational domain.⁴²

The body-fixed coordinate system could be used to define the pitch, roll, and yaw motions of the specimen. In our simulation, the body orientation of the dragonfly is fixed within the computational domain and the head-thorax-abdomen assembly is treated as a solid body. The wing-fixed coordinate system is flapping (rotates around the wing pivot according to the positional angle) together with the wing to give a convenient way to describe the change in the positional angle (ϕ), the feathering angle (α), and the deviation angle (χ) in relation to the stroke plane [Fig. 3(a)]. The stroke plane is the plane in which the wing is flapping.

The positional angle (ϕ) defines the wing's position within the stroke plane. The origin of the positional angle is the wing pivot. The positional angle is zero when the wing's spanwise axis is parallel

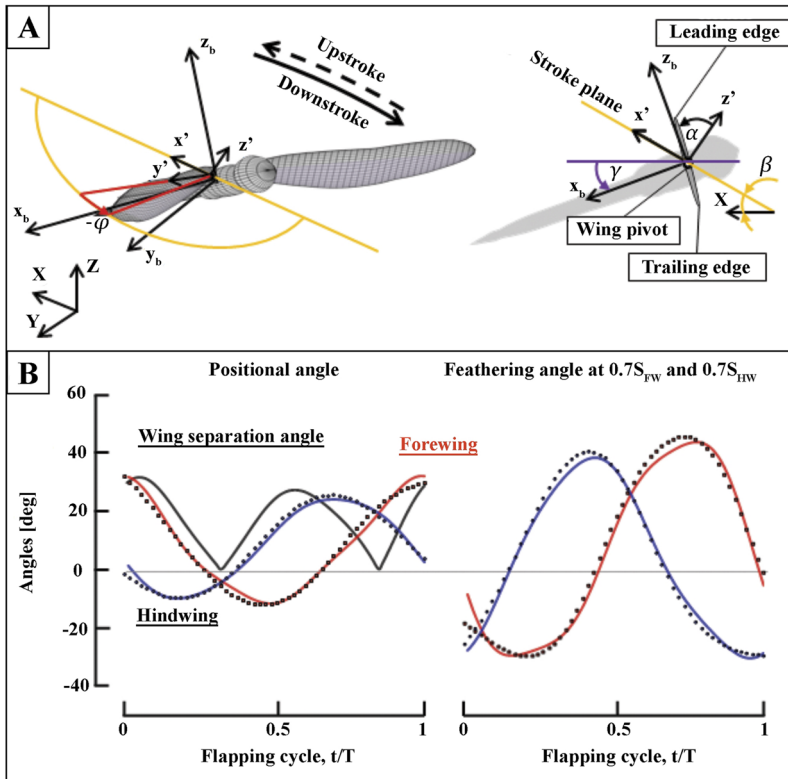


FIG. 3. (a) The definition of the kinematic and geometric angles of the free-flying dragonfly: the stroke plane is defined as the x' - y' plane. The stroke plane angle is β . The wing positional angle is φ . The feathering angle is α . The body angle is γ . (b) Wing kinematics under moderately ascending, free-flight adopted for the numerical simulation (dots represent the measured positions, continuous line is the fitted curve, S_{HW} and S_{FW} stands for the wingspan of hind- and forewing). t/T is the dimensionless time, where T is the period and $t = 0$ at the start of the downstroke of the forewing in the first flapping cycle.

to the principal plane of the dragonfly body sideways. The feathering angle (α) defines a wing chord's pitching around the spanwise axis. The feathering angle is zero when the wing is perpendicular to the stroke plane. The deviation angle (χ) defines the wings motion out of the stroke plane during a flapping cycle. The stroke plane angle (β) is the angle between the stroke plane and the horizontal axis in the global coordinate system [Fig. 3(a)]. The body angle (γ) is the angle between the axis of the dragonfly body and the horizontal axis in the global coordinate system [Fig. 3(a)]. The experimentally measured flapping kinematics of the dragonfly can be well described with two angles around the wing pivot, as the deviation angle (χ) is negligible. The measured wing kinematics is presented in Fig. 3(b).

For the analysis of the flow field around the dragonfly model, we used a CFD solver, based on a finite volume method and a fortified Navier–Stokes solver for a multi-blocked, overset-grid system.^{42,43} The computational tools based on these techniques have been utilized and validated in numerous applications, including some of the case studies presented in the reference work of Shyy *et al.*² The numerical solver⁴² was used with permission and without further alteration of the source coding. The numerical model is based on the measured dynamic deformation of the wings of a free-flying dragonfly in one flapping cycle of the selected flight. Ensuring good continuity of the kinematic parameters in the simulation, fitted curves were adopted by using the third order of Fourier series for the periodic computation as described in Ref. 42. In Fig. 3(b), the measured positional and feathering angles are

presented together with the fitted curves that were adopted for the simulation.

The governing equations of the numerical solver are the three-dimensional, incompressible, unsteady Navier–Stokes equations written in strong conservation form for mass and momentum. The artificial compressibility method is used by adding a pseudo-time derivative of pressure to the equation of continuity. For an arbitrary deformable control volume $V(t)$, the non-dimensionalized governing equations are

$$\int_{V(t)} \left(\frac{\partial \mathbf{Q}}{\partial t} + \frac{\partial \mathbf{q}}{\partial \tau} \right) dV + \int_{V(t)} \left(\frac{\partial \mathbf{F}}{\partial x} + \frac{\partial \mathbf{G}}{\partial y} + \frac{\partial \mathbf{H}}{\partial z} + \frac{\partial \mathbf{F}_v}{\partial x} + \frac{\partial \mathbf{G}_v}{\partial y} + \frac{\partial \mathbf{H}_v}{\partial z} \right) dV = 0, \quad (1)$$

where bold letters are used to denote matrices,

$$\mathbf{Q} = \begin{bmatrix} u \\ v \\ w \\ 0 \end{bmatrix}, \quad \mathbf{q} = \begin{bmatrix} u \\ v \\ w \\ p \end{bmatrix}, \quad \mathbf{F} = \begin{bmatrix} u^2 + p \\ uv \\ uw \\ \lambda u \end{bmatrix}, \quad \mathbf{G} = \begin{bmatrix} vu \\ v^2 + p \\ vw \\ \lambda v \end{bmatrix}, \quad \mathbf{H} = \begin{bmatrix} wu \\ wv \\ w^2 + p \\ \lambda w \end{bmatrix},$$

$$\mathbf{F}_v = -\frac{1}{\text{Re}} \begin{bmatrix} 2u_x \\ u_y + v_x \\ u_z + w_x \\ 0 \end{bmatrix}, \quad \mathbf{G}_v = -\frac{1}{\text{Re}} \begin{bmatrix} v_x + u_y \\ 2v_x \\ v_z + w_y \\ 0 \end{bmatrix}, \quad \mathbf{H}_v = -\frac{1}{\text{Re}} \begin{bmatrix} w_x + u_z \\ w_y + v_z \\ 2w_z \\ 0 \end{bmatrix}.$$

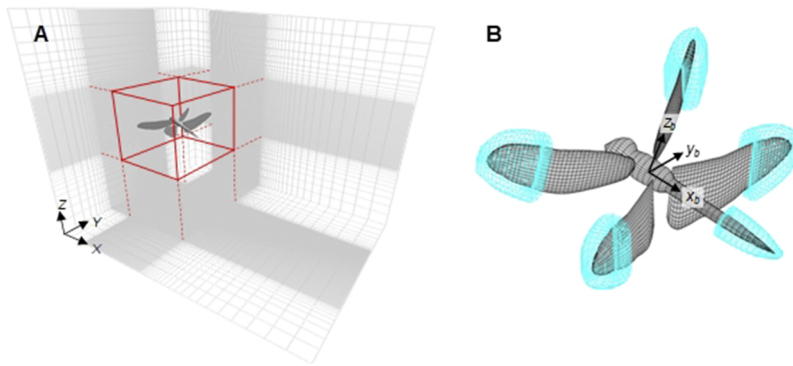


FIG. 4. Grid and coordinate systems: (a) global grid block and (b) grids of a dragonfly body and wings.

In the above, λ is the pseudo-compressibility coefficient; p is pressure; u , v , and w are velocity components in the Cartesian coordinate system X , Y , and Z ; t denotes physical time, while τ is pseudo-time; and Re is the Reynolds number. The term q associated with the pseudo-time is designed for an inter-iteration at each physical time step, which will vanish when the divergence of velocity is driven to zero to satisfy the equation of continuity.

In this study, the computational domain was an $8S_{FW} \times 6S_{FW} \times 6S_{FW}$ sized Cartesian grid [Fig. 4(a)] in which the body grid and the two fore- and hind-wing grids (flyer blocks) are immersed [Fig. 4(b)]. The Cartesian grid has two sub-regions: clustering region which has small, uniform grid spacing [highlighted by a red square on Fig. 4(a)] and the global cluster that is gradually refined toward the center of the computational domain. The uniform grid spacing is set to be $0.15C_f$ in the basic model. The outer boundaries of the flyer blocks are immersed in the clustering region to prevent loss of accuracy due to the interpolation between the global block and flyer blocks. The numbers of grid points in $i \times j \times k$ are the following: the global grid is $103 \times 109 \times 93$; the body grid is $35 \times 35 \times 9$; the two fore- and hindwing grids are $37 \times 37 \times 17$ each.

The time step for the computation is fixed at $dt = 0.0005$ corresponding to about 1.37×10^{-5} s, that is about 2000 step for one flapping cycle of a fore- or hind wing. With this value, the convergence of the flow field was ensured. The boundary conditions for the velocity and the pressure are given as: (1) at upstream the velocity is the inflow while pressure is set to zero and (2) at downstream zero-gradient condition is taken for both velocity and pressure.⁴² On the body surface, the no-slip condition is used for the velocity components.⁴²

The model parameters are summarized in Table I. The computation is done in the laminar flow regime; no turbulence modeling was implemented. Note that the head, thorax, and tail ensemble is treated as one rigid body, and the flexible fore- and hind-wing models are reconstructed based on the coordinates of the landmarks on the flapping wings recorded during the experiment as in Ref. 44. In the computational model, the dragonfly body is fixed in the computational domain and components of an added inflow are 0.63 m/s in horizontal and -0.49 m/s in the vertical direction in the global coordinate system that is based on the measured flight speed and direction of the free-flying dragonfly (slightly emerging slow forward flight), to account for the free-flight condition. The added inflow is simplified by using the average

value. The slight changes in flight speed are not considered in this study.

$$(U_{ref} = 2\phi S_{FW}f) \quad (2)$$

$$(k = 2\pi f C_f / U_{ref}) \quad (3)$$

$$(Re = U_{ref} C_f / \nu) \quad (4)$$

C. Verification and validation of the computational model

The self-consistency of the solver for low Reynolds number studies was assessed previously.⁴² To ensure sufficiently qualified grids as well as a reasonable computational time, the $N \times N \times N$ grid size can be derived,

$$N = L / \sqrt{Re}. \quad (5)$$

Here, L is the mean length of the wing in the streamwise direction. The applied grid in the current study is finer than what is necessary. To observe the influence of the grid resolution, the time step, and the domain size on the computational results, we used the

TABLE I. Parameters used for the computational analysis.

Mean chord length (fore), C_f (mm)	7.94
Mean chord length (hind), C_h (mm)	11.44
Wing length (fore), S_{FW} (mm)	43.4
Wing length (hind), S_{HW} (mm)	40.1
Flapping frequency, f (Hz)	36.4
Flapping amplitude, ϕ (rad)	0.77
Stroke plane angle (fore) β_f (deg)	34.5
Stroke plane angle (hind) β_h (deg)	37.9
Body angle γ (deg)	20
Density of air, ρ (kg/m ³)	1.225
Kinematic viscosity of air, ν (m ² /s)	1.5×10^{-5}
Reference velocity, U_{ref} (m/s)	2.42
Reduced frequency, k (-)	0.37
Reynolds number (fore), Re_{FW} (-)	1288
Reynolds number (hind), Re_{HW} (-)	1714

TABLE II. The computational system parameters.

Case study	Domain size ($X \times Y \times Z$)	dt [-]	Global grid ($I \times j \times k$)	Body grid ($I \times j \times k$)	Wing grids ($I \times j \times k$)	Cycle-averaged vertical force (mN)
Basic	$8S_{FW} \times 6S_{FW} \times 6S_{FW}$	0.000 5	$103 \times 109 \times 93$	$35 \times 35 \times 9$	$37 \times 37 \times 17$	3.67
Fine grid	$8S_{FW} \times 6S_{FW} \times 6S_{FW}$	0.000 5	$141 \times 153 \times 125$	$41 \times 41 \times 13$	$47 \times 47 \times 21$	3.76
Coarse grid	$8S_{FW} \times 6S_{FW} \times 6S_{FW}$	0.000 5	$79 \times 81 \times 73$	$27 \times 27 \times 7$	$27 \times 27 \times 13$	3.62
Fine step	$8S_{FW} \times 6S_{FW} \times 6S_{FW}$	0.000 25	$103 \times 109 \times 93$	$35 \times 35 \times 9$	$37 \times 37 \times 17$	3.68
Coarse step	$8S_{FW} \times 6S_{FW} \times 6S_{FW}$	0.001	$103 \times 109 \times 93$	$35 \times 35 \times 9$	$37 \times 37 \times 17$	3.66
Enlarged domain	$10S_{FW} \times 8S_{FW} \times 8S_{FW}$	0.000 5	$131 \times 145 \times 125$	$35 \times 35 \times 9$	$37 \times 37 \times 17$	3.66

base model along with five additional systems. The system parameters are summarized in Table II. The two fore- and hindwing grids are the same number in this computation.

Figure 5 shows the total vertical forces acting on the dragonfly body and its four wings in the dependency study. The vertical forces of the fine and the coarse grid systems are slightly increased and decreased, respectively, both around $t/T = 3.3$. The other systems maintain the same value with the basic model. The total cycle-averaged value of the vertical force considering the body ensemble and all four wings is shown in Table II. Although there is some difference between the cycle-averaged vertical force of the finer and the basic grid systems, its effect on the discussed flow features and on the spanwise variance of aerodynamic forces is minor. The basic grid system was adopted for this study, since the fine grid system would be computationally more expensive.

Second, the results of the numerical study were compared with flow field measurements of live free-flying dragonflies at multiple spanwise positions by TR-PIV. The results were also cross-checked and found to show reasonable qualitative agreement with previous tethered PIV flow field measurements of the same dragonfly species.³⁷

The flow features of a tethered dragonfly along its wingspan are presented in the inner-, transition- and outer-regions that are shown to have distinct features by tethered flow measurement.³⁷ In the case of a quarter cycle hindwing lead flapping, an LEV-LEV interaction dominated the inner span. Differently, in the outer span, a vortex capture mechanism, in which case the hindwing captures the shed vortex of the forewing, was reported.³⁷ Closest to the root, a transition region is formed, where negligible inter-wing interaction takes place due to the small distance between the ipsilateral wings.³⁷ A second transition region is formed between the inner span and the outer span regions, where the downwash of the forewing is the dominant interaction feature observed.³⁷

Here, we compare the results of the numerical model with free-flight flow measurement, focusing on the features presented in the referred work. We emphasize that the numerical study models one particular flight that has been measured via high-speed video, and it was not the intention of this study to case by case preset the boundary conditions of the numerical study to match exactly those of the PIV free-flight measurements. Furthermore, the numerical code does not feature a fully coupled fluid-structure interaction modeling, but the time-dependent wing-shape morphology is prescribed. Due to these reasons, an exact match between the measured and modeled flow fields is not expected; however, the most characteristic

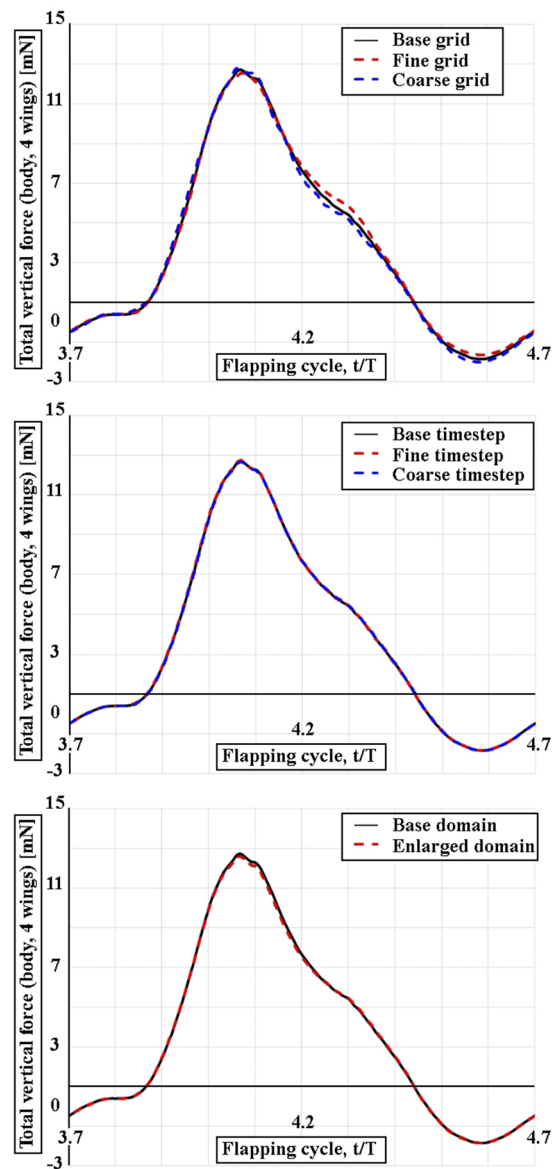


FIG. 5. Sensitivity analysis on grid points, time step, and domain size.

features can be identified and compared qualitatively to help elucidate the overall physical mechanisms. Several free-flight trials were conducted with multiple specimens. In the following, we present cases where the results were the clearest, the specimen flew quasi-horizontally, and the wing positions and measurement sections were adequate to show the flow features. We selected the time instants when the dominant flow features³⁷ are clearly present, case by case, for each measured region. In Figs. 6 and 7, the flow features during the downstroke and upstroke of the hindwing are presented, respectively. In the figures showing the flow fields, F and H subscripts refer to forewing and hindwing vortices, respectively, and asterisks mark a captured vortex.

In Fig. 6, the dominant interaction features³⁷ are shown during the downstroke of the hindwing; left column shows the results of the numerical simulation, while the right column shows the results of the flow measurements. Figures 6(a) and 6(b) present the flow in the inner region of the hindwing. In Fig. 6(a), the upstroke

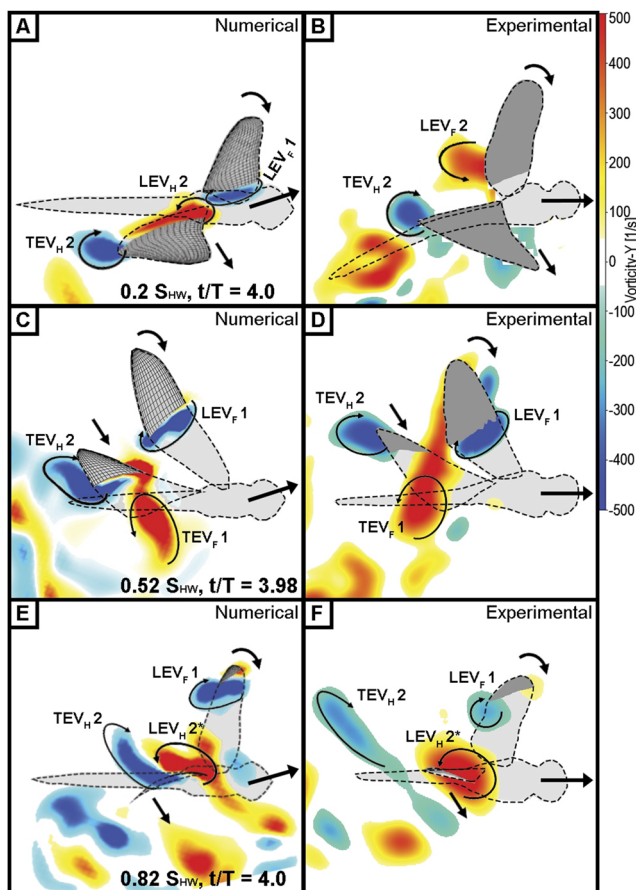


FIG. 6. Vorticity contours at three spanwise regions at time instants when the dominant interaction features can be clearly observed. Numerical (a), (c), and (e), and experimental (b), (d), and (f) results of PIV measurement. t/T is the dimensionless time, where T is the period and $t = 0$ at the start of the downstroke of the forewing in the first flapping cycle. S_{HW} stands for the wingspan of the hindwing. Arrows indicate the wing motion and flight direction.

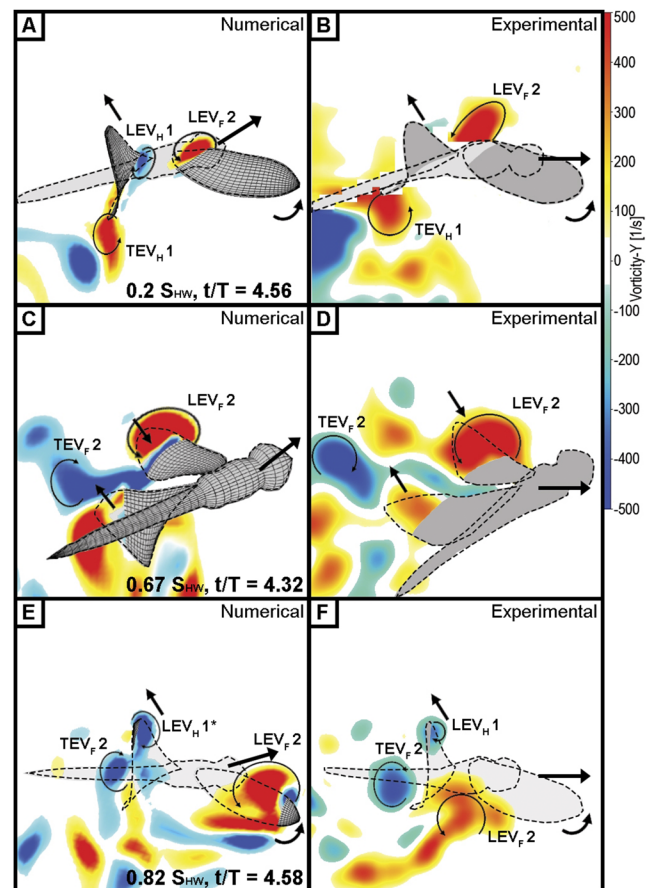


FIG. 7. Vorticity contours at three spanwise regions at time instants when the dominant interaction features can be clearly observed. Numerical (a), (c), and (e) and experimental (b), (d), and (f) results of PIV measurement. t/T is the dimensionless time, where T is the period and $t = 0$ at the start of the downstroke of the forewing in the first flapping cycle. S_{HW} stands for the wingspan of the hindwing. Arrows indicate the wing motion and the flight direction.

formed LEV of the forewing (LEV_{F1}) sheds downstream, while the forewing is pitching downward. This vortex (LEV_{F1}) influences the formation of the downstroke hindwing LEV (LEV_{H2}). In tethered flow measurements, vortex synergy was found between the fore- and hindwing LEV.³⁷ Here, a similar synergy takes place between the LEVs (LEV_{F1} and LEV_{H2}). The shedding hindwing TEV (TEV_{H2}) can also be observed. Figure 6(b) shows the measured flow around the wings of a free-flying dragonfly in the inner region. Figure 6(b) shows a hindwing TEV (TEV_{H2}) of comparable size and strength with the one observed in Fig. 6(a); however, due to the strong reflection from the specimen's body, we could not measure the flow in the area where the LEVs are expected to be found. A difference from the numerical model is a LEV (LEV_{F2}) that is shedding above the forewing. This LEV is formed by the forewing due to a brief descent of the dragonfly that highly altered the effective angle of attack of the forewing prior to the presented flapping cycle.

Figures 6(c) and 6(d) present the flow in the transitional region. In both cases, the shed forewing vortex (TEV_{F_1}) moves downstream below the downstroking hindwing. Neither LEV–LEV synergy nor vortex capture is observed. The overall flow features, the vortex positions, strength, and size are similar in the case of the numerical model [Fig. 6(c)] and the measurement [Fig. 6(d)].

Figures 6(e) and 6(f) present the flow near the wingtips. The most dominant feature that can be observed in both the numerical results [Fig. 6(e)] and the measured [Fig. 6(f)] flow is that the downstroking hindwing captures elements of the shed forewing TEV (noted as $LEV_{H_2^*}$). This pattern was observed by tethered measurements previously.³⁷ The shed forewing and hindwing TEVs (LEV_{F_1} and TEV_{H_2}) are positioned slightly more downstream in the case of the measurement probably due to the different flight direction and speed in the presented cases. The overall flow features again show a good qualitative agreement between the two cases.

In Fig. 7, the dominant interaction features³⁷ are shown during the upstroke of the hindwing; left column shows the results of the numerical simulation, while the right column shows the results of the flow measurements. Figures 7(a) and 7(b) show the flow in the inner region. Figure 7(a) shows the LEVs of the forewing (LEV_{F_2}) and the hindwing (LEV_{H_1}) closely positioned, allowing a vortex synergy³⁷ to take place. A TEV of the hindwing (TEV_{H_1}) can also be observed in Figs. 7(a) and 7(b). The measured flow of the free-flying dragonfly [Fig. 7(b)] shows the forewing LEV (LEV_{F_2}) and the hindwing TEV (TEV_{H_1}) similarly positioned as in the case of the numerical results. Again, due to the reflection from the specimen's body, the hindwing LEVs existence could not be determined.

In Figs. 7(c) and 7(d), the forewing LEV (LEV_{F_2}) and the forewing TEV (TEV_{F_2}) positions and the vorticity magnitudes are reasonably similar. The forewing TEV sheds downstream above the hindwing without an apparent LEV–LEV interaction in both cases.

In the outer region, the dominant interaction mechanism is a wake vortex capture by the hindwing.³⁷ Figure 7(e) presents the formation of an upstroke hindwing LEV ($LEV_{H_1^*}$) by the partial capturing of the shed forewing TEV (TEV_{F_2}). The forewing downstroke LEV (LEV_{F_2}) also can be observed in Fig. 7(e). Differently, during free-flight measurement [Fig. 7(f)], capture of the upstroke vortex did not happen, but a weak upstroke LEV is formed by the hindwing (LEV_{H_1}). Moreover, in Fig. 7(f), the forewing vortices (FDT and LEV_{F_2}) are found more downstream than in the case of the numerical results. These differences can be explained with the prior descending and level flight of the measured specimen vs the slight ascending flight of the simulated dragonfly. The similar influence of flight direction to the vortex capture in the outer span has been discussed previously.³⁷

III. RESULTS AND DISCUSSION

A. Flight behavior and the dynamic shape deformation of the dragonfly wings in free-flight

In the experiments, after release, the dragonfly starts flapping immediately. It orients itself to the desired flight direction within a short period of time and then proceeds forward with steady, hindwing lead out-of-phase strokes. The variance of the flapping kinematics of the free-flying specimens was presented in our previous

study.³⁷ This general flight sequence has four possible stages: recovering maneuvers, slight descending or ascending, and level-flight (Fig. 8). Interaction features could be present at any of these four stages depending on the actual stroke kinematics and flight velocity of the dragonfly.

While in motion, the wings are passively cambering and twisting according to the pressure gradients and inertial forces acting on the flexible membrane. The spanwise camber is less substantial due to the strong leading edge and the corrugated wing structure. Figure 9 shows the measured feathering angle and the chordwise camber of the fore- and hind-wing at four spanwise cross sections. The camber is defined as the ratio between the distance of the leading and trailing edges and the deflection at the middle of the chord. We can see from the graphs that the twisting of the wings gradually increases toward the tip; however, the chordwise camber is related to the local chord width. The gradual twisting of the wing causes the local angle of attack to gradually decrease toward the wingtip. It is reasonable to assume that above a certain flight speed, the wing twisting together with the streamwise component of the incident flow will result in vortex breakdown²⁸ at the outer span. The chordwise cambering helps preserve the LEV on the pressure side of the flapping wing of a live dragonfly during stroke reversal.³⁷

B. Aerodynamic performance of the wings

1. Systems-level approach

Aerodynamic forces derived from the results of the numerical model are first evaluated on a systems level. All the forces are presented in the body-fixed coordinate system (x_b - y_b - z_b). Figure 10(a) presents the aerodynamic forces in the global coordinate over one complete cycle in tandem operation of the wings. The total forces of the fore- and hindwing in the vertical and horizontal axis are also given in Fig. 10(a).

Both wings are generating thrust at the upstroke and lift at the downstroke. The total vertical force is negative only when both the wings are upstroking while the total thrust force oscillates with twice the frequency of the flapping frequency and shows the highest negative value at the time when both wings are in their downstroke. Interestingly, only the hindwing generates substantial drag in the second

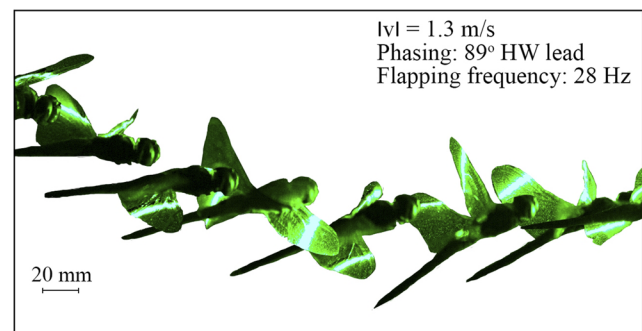


FIG. 8. A representative free-flight sequence (cut from the recorded frames of PIV flow measurement). $|v|$ is the average flight speed of the dragonfly.

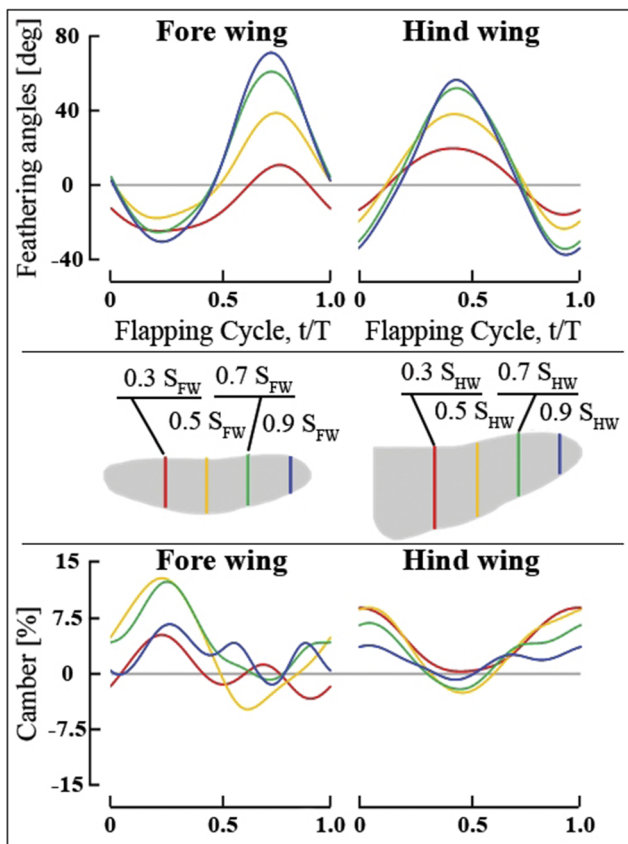


FIG. 9. The dynamic deformation of the wings throughout a flapping cycle at four distances. t/T is the dimensionless time, where T is the period and $t = 0$ at the start of the downstroke of the forewing in the first flapping cycle. S_{HW} and S_{FW} stand for the wingspan of the hind- and forewing.

half of its downstroke [Fig. 10(a)]. From the results in Fig. 10(b) (t/T 4.1 to 4.2), we can see that the drag is, in part, attributed to the interaction with the forewing. *Sympetrum frequens*, a dragonfly species similar in size to those in this study, was filmed in slow forward flight and the aerodynamic forces during a flapping cycle were calculated using momentum theory, blade element theory, and a numerical method modified from the local circulation method.⁴⁵ This study also reports that most of the thrust force is generated during upstroke and lift during the downstroke of both wings, and the largest drag occurs when both wings are upstroking. Differently in their study, the forewing generated more drag than the hindwing, which might be the result of slightly different wing geometries and flapping kinematics. Free-flight of *Pachydiplax longipennis*, another species comparable with the one in our investigation, has been recorded to numerically study upright and inverted flight.⁴⁶ We refer to the lift and thrust during normal upright flight for the following comparison. The time histories presented are in good agreement with the current results; however, the force magnitudes are more moderate and in their case the hindwing produces no drag during the second half of its downstroke.⁴⁶ These discrepancies could be

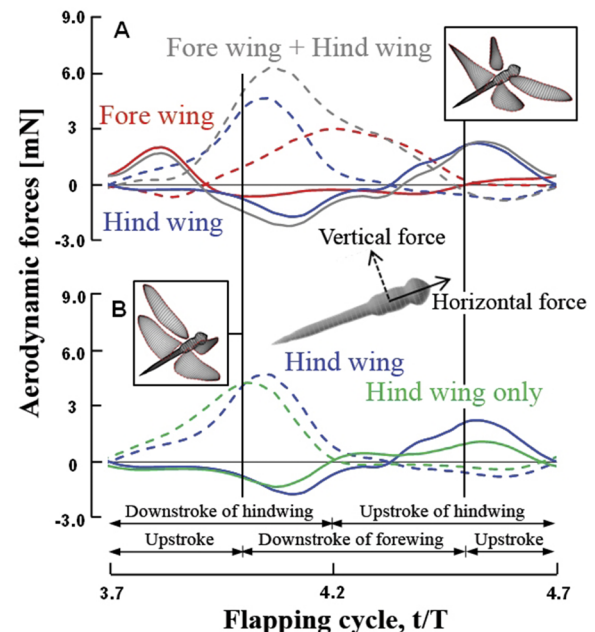


FIG. 10. (a) Horizontal (solid lines) and vertical (dashed lines) forces of the flexible wing numerical model over a cycle in tandem wing operation. (b) Horizontal (solid lines) and vertical (dashed lines) forces of the hindwing with and without the influence of the forewing. (The results are derived from the numerical study.) t/T is the dimensionless time, where T is the period and $t = 0$ at the start of the downstroke of the forewing in the first flapping cycle.

explained by the slightly different flight direction (and body orientation) and flapping kinematics of the specimen in their work. Nevertheless, in comparison with our investigations, the reported magnitude of forces is within an acceptable margin, considering the differences in flight kinematics and wing geometries in the above studies.

Figure 10(b) shows the effect of the interaction on the hindwing force generation by comparing the vertical and horizontal forces generated by the hindwing with and without the effect of the forewing. From the graphs, it is apparent that the interaction increases the vertical and horizontal peak forces. Three parts of the flapping cycle are distinct. From t/T 3.7 to 4, the hindwing is in its first half of downstroke, during which, the generated lift decreases while the thrust is unchanged. In the second half of the downstroke, and during the beginning of the upstroke of the hindwing (t/T 4 to 4.4), the interaction redistributes the generated forces more vertically, more lift and less thrust generated. Finally, at the upstroke phase of the hindwing, the interaction is advantageous, more thrust is generated while the lift is decreased slightly.

Furthermore, total cycle-averaged horizontal and vertical forces in the global coordinate are 1.15 mN and 3.54 mN, respectively. Considering that the measured weight of the dragonfly after the experiment was 3.28 mN, our computational model generates slightly more lift than what is needed for weight support. In addition, the positive horizontal value manifests from the insufficient force for flying with the measured flight speed. In other words, the total force

vector of the numerical model is tilted backward, resulting in an upward acceleration instead of steady emerging flight. The slight discrepancy in the force values can be attributed to the simplifications of the model.

2. Span-resolved approach

To investigate how the dragonfly wing's force generation varies over the span, we resolved the span into 10 regions sideways from the hindwing root to the wingtip. We conceptually focus on how the interaction affects the force generation by the hindwing. As previously shown, at an approximately quarter cycle hindwing lead phasing of the wings, the interaction has negligible effect on the forewing.^{16,19,20,31,33,35} The following flow and force evaluation is based on the numerical results.

Figures 11(a) and 11(b) show the horizontal force time histories, while Figs. 11(c) and 11(d) show the vertical force time histories of the fore- and hind wing resolved to the wingspan while the wings are in tandem operation. The magnitudes of the generated forces show substantial differences over the span. From the graphs, we can see that the highest aerodynamic forces are generated in the region of $0.4-0.6 S_{HW}$ and S_{FW} , distributed evenly around the midspan except in the case of the horizontal force generated by the forewing [Fig. 11(a)] where it is slightly shifted toward the outer span. The horizontal force generated by the forewing is largest in the region of $0.5-0.8 S_{FW}$. These results contradict the assumption that the generated lift could be gradually increasing toward the wingtip, as expected in the case of a wing that sustains an attached LEV with gradually increased circulation toward the wingtip.³⁹

In the case of the forewing, the temporal change in the aerodynamic forces resolved to the wingspan is very similar, only the force magnitudes are different. The invariant time histories of forces generated along the wingspan of the forewing confirm that while in an approximately quarter cycle hindwing lead setup the forewing is not substantially affected by the hindwing. Considering the time courses of forces resolved to the wingspan, these are very different in the case of the hindwing horizontal force component, while there is only a slight difference in the case of vertical force generation. The span-wise variation in the force generation of the hindwing is likely the result of interaction with the forewing.

To further investigate the interaction effect on the hindwing, we numerically calculated force generation in the case of solo vs tandem operation. Figures 12(a) and 12(b) show the horizontal force and (c) and (d) the vertical force time histories of the hindwing in tandem and in solo operation.

First, we investigate the initial part of the stroke of the hindwing. The interaction decreases the generated vertical force during the first third of the downstroke [Fig. 12(c) vs Fig. 12(d) at $t/T = 3.8$ for instance]; on the other hand, there is no negative vertical force generated during the first third of the upstroke [Fig. 12(c) vs Fig. 12(d) at $t/T = 4.3$ for instance] in the region that spans from $0.4 S_{HW}$ to $0.8 S_{HW}$. Less drag (negative horizontal force) occurs in the first third of the downstroke ($t/T = 3.8$), while the largely decreased force generation adds drag during the first third of the upstroke ($t/T = 4.3$). Again, the interaction is most prominent in the region of $0.4 S_{HW}$ to $0.8 S_{HW}$.

During the rest of the up- and downstroke, there is a vertical force amplification (both negative and positive) and it is present in

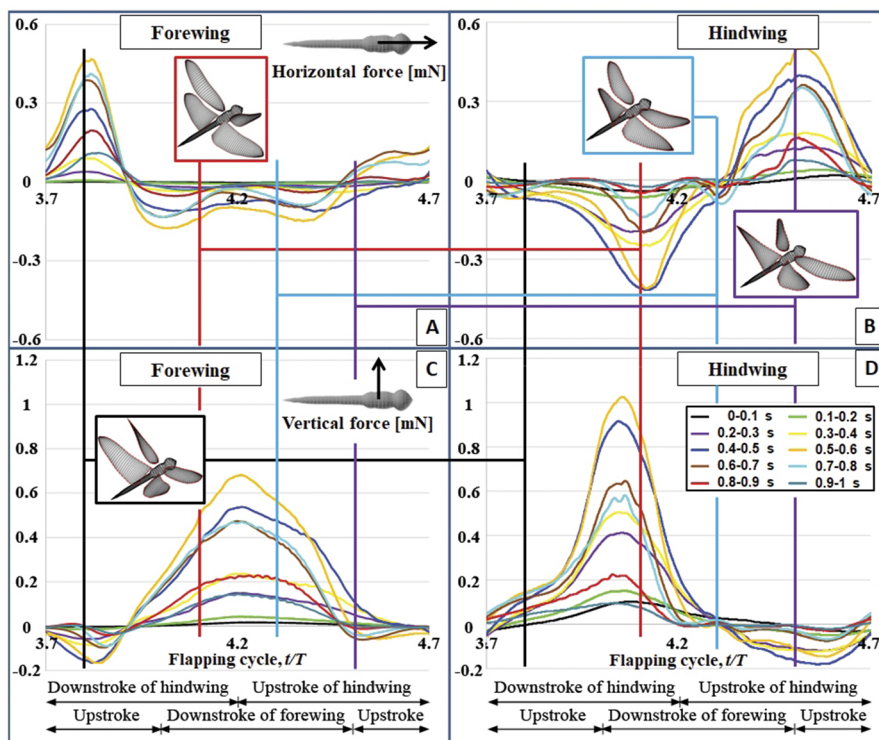


FIG. 11. Horizontal [(a) and (b)] and vertical [(c) and (d)] forces acting on the hindwing and forewing in tandem operation, resolved along the hindwing span (results derived from the numerical study). t/T is the dimensionless time, where T is the period and $t = 0$ at the start of the downstroke of the forewing in the first flapping cycle. S_{HW} and S_{FW} stands for the wingspan of the hind- and forewing.

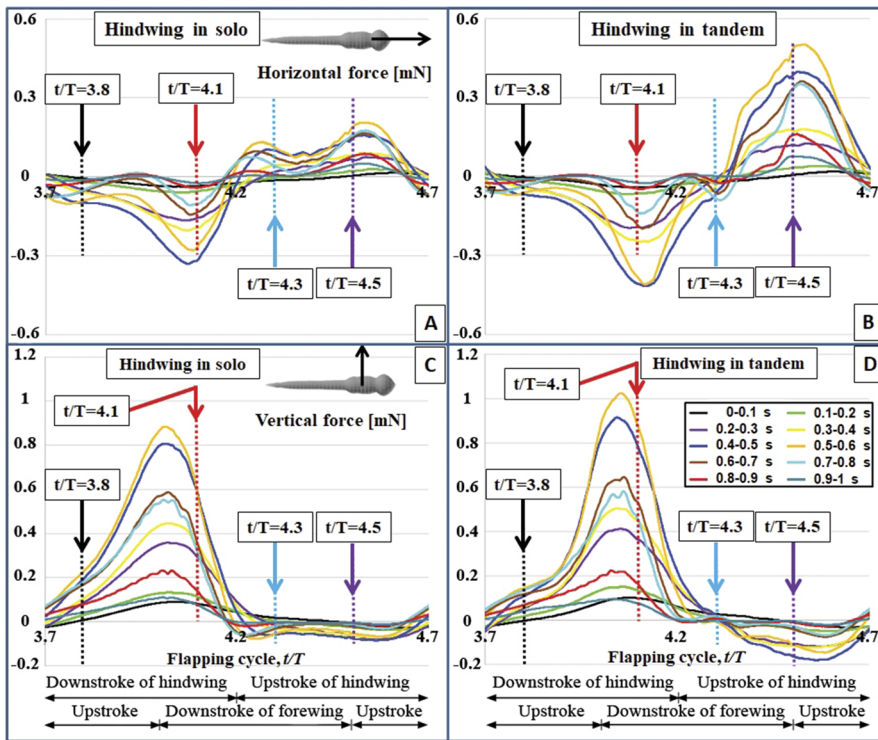


FIG. 12. Horizontal [(a) and (b)] and vertical [(c) and (d)] forces acting on the hindwing in tandem vs solo operation, resolved along the hindwing span (results derived from the numerical study). t/T is the dimensionless time, where T is the period and $t = 0$ at the start of the downstroke of the forewing in the first flapping cycle. S_{HW} and S_{FW} stand for the wingspan of the hind- and forewing.

the region of $0.2 S_{HW}$ to $0.6 S_{HW}$ and strongest at the midspan region of about $0.4 S_{HW}$ to $0.6 S_{HW}$ [Fig. 12(c) vs Fig. 12(d) at $t/T = 4.1$ and 4.5 for instance]. Regarding the horizontal force modulation, there is a large gain during the upstroke of the hindwing [Fig. 12(a) vs Fig. 12(b) at $t/T = 4.5$ for instance], which results most prominently from the interaction in the region that spans from $0.2 S_{HW}$ to $0.9 S_{HW}$. During the downstroke [Fig. 12(a) vs Fig. 12(b) at $t/T = 4.1$ for instance], the drag amplification is less intense and limited to a smaller region that spans from $0.4 S_{HW}$ to $0.6 S_{HW}$.

To understand the underlying flow phenomena that results in force modulation on the hindwing, we have visualized the flow at critical time instants: $t/T = 3.8, 4.1, 4.3$, and 4.5 (marked in Figs. 11 and 12). A supplementary video of the iso-surfaces of $Q = 1.2$, streamlines and non-dimensional absolute velocity in the midspan, for two complete cycles can be accessed in Fig. 13 (Multimedia view). In Figs. 14 and 15, the flow features at the beginning of the hindwing down- and upstroke ($t/T = 3.8$ and 4.3) are shown in detail. Figures 14(a) and 15(a) show the iso-surfaces of Q -criterion in hindwing solo operation; furthermore, iso-surfaces of Q -criterion, velocity magnitude and streamlines at mid-span [Figs. 14(b) and 15(b)], are shown in tandem operation. We also present the non-dimensionalized pressure distribution on the wing surfaces in solo [Figs. 14(c), 14(e), 15(c), and 15(e)] and tandem mode [Figs. 14(d), 14(f), 15(d), and 15(f)].

Figure 14 shows the flow features and the pressure distribution on the surfaces of the wings at the beginning of the downstroke of the hindwing ($t/T = 3.8$). Confirming the trends of force modulation in Fig. 12 at $t/T = 3.8$, the pressure distribution clearly shows that

interaction in the outer span ($0.4 S_{HW}$ to $0.8 S_{HW}$) results in the decreased force generation in tandem mode. At $t/T = 3.8$, the hindwing LEV of the upstroke (LEV_{H_1}) is shedding at the bottom surface of the wing. The forming downstroke hindwing LEV (LEV_{H_2}) is also visible in Fig. 14(b). Compared with the iso-surfaces in single hindwing operation [Fig. 14(a)], we can see that the shedding upstroke formed LEV of the hindwing is enhanced while forming of the downstroke LEV is delayed in tandem operation. The change

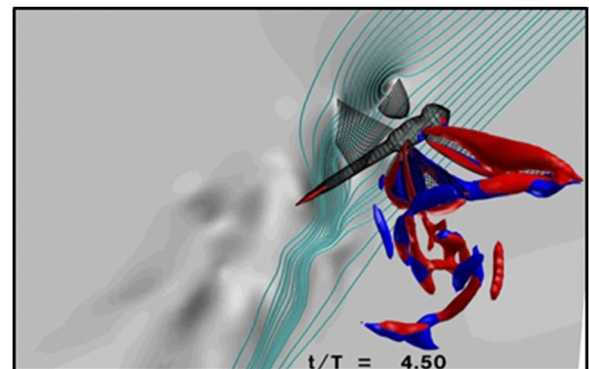


FIG. 13. The iso-surfaces of Q -criterion ($Q = 1.2$), streamlines and non-dimensional absolute velocity in the midspan, for two complete cycles. Multimedia view: <https://doi.org/10.1063/1.5145199.1>

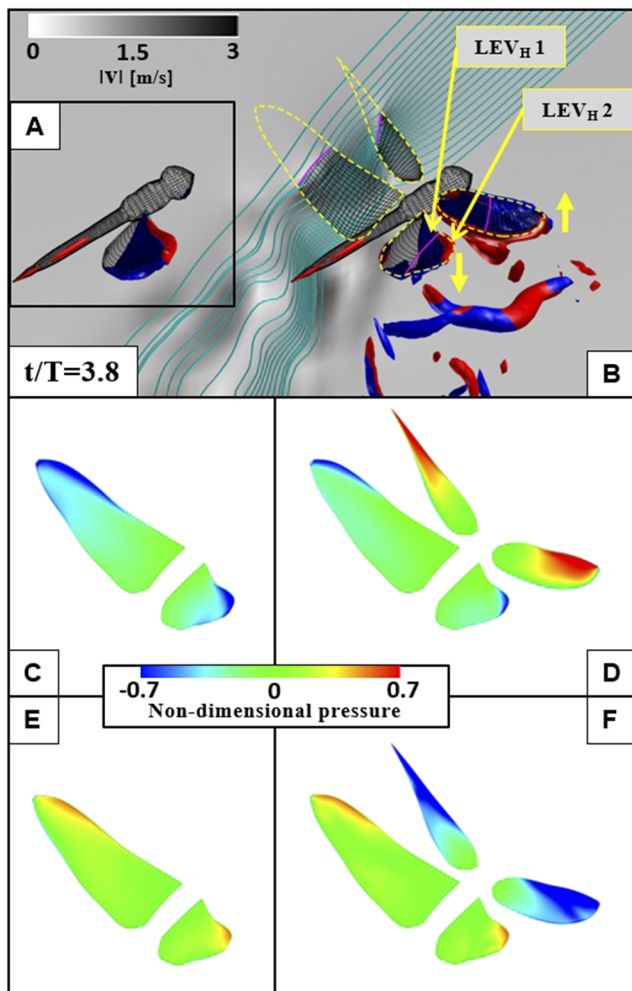


FIG. 14. (a) Iso-surfaces of Q -criterion ($Q = 1.2$ colored by Y -vorticity to indicate direction; red is positive and blue is negative), (b) iso-surfaces of $Q = 1.2$, streamlines and non-dimensional absolute velocity; and pressure distribution on the top [(c) and (d)] and bottom [(e) and (f)] wing surface at $t/T = 3.8$ in solo (a)–(c)–(e) and tandem (b)–(d)–(f) mode. The wings' motion is indicated by yellow arrows, and the midspan is highlighted by the pink line for reference. t/T is the dimensionless time, where T is the period and $t = 0$ at the start of the downstroke of the forewing in the first flapping cycle. $|\mathbf{v}|$ is the velocity magnitude at the mid-span cross section.

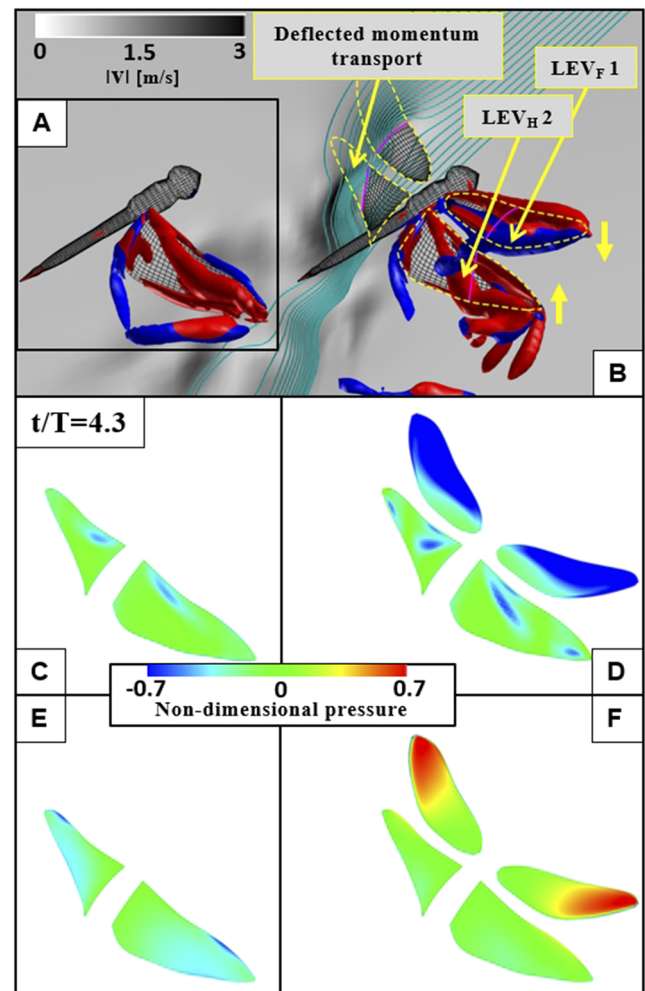


FIG. 15. (a) Iso-surfaces of Q -criterion ($Q = 1.2$ colored by Y -vorticity to indicate direction; red is positive and blue is negative), (b) iso-surfaces of $Q = 1.2$, streamlines and non-dimensional absolute velocity; and pressure distribution on the top [(c) and (d)] and bottom [(e) and (f)] wing surface at $t/T = 4.3$ in solo (a)–(c)–(e) and tandem (b)–(d)–(f) mode. The wings' motion is indicated by yellow arrows, and the midspan is highlighted by the pink line for reference. t/T is the dimensionless time, where T is the period and $t = 0$ at the start of the downstroke of the forewing in the first flapping cycle. $|\mathbf{v}|$ is the velocity magnitude at the mid-span cross section.

in the vortex strength results in a lower pressure difference between the pressure and suction side of the hindwing [Figs. 14(c) and 14(e) vs Figs. 14(d) and 14(f)] and explains the decreased force generation of the hindwing in tandem operation at $t/T = 3.8$ (Fig. 12). The reason for these changes can be traced back to the interaction with the shed forewing TEV (vortex capture) earlier in the stroke cycle [see Fig. 13 (Multimedia view) $t/T = 4.46$ to 4.56]. The vortex capture mechanism will be further discussed later.

Figure 15 shows the flow features and the pressure distribution on the surfaces of the wings at the beginning of the upstroke of the hindwing ($t/T = 4.3$). Observing the iso-surface of Q -criterion of the hindwing LEV in Fig. 15(a) vs Fig. 15(b) and the pressure

distributions in solo vs tandem operation [Figs. 15(c) and 15(e) vs Figs. 15(d) and 15(f)], we can see that the shedding downstroke LEV (LEV_{H2}) contributes substantially to the aerodynamic force modulation. This LEV is enhanced and positioned closer to the pressure surface of the upstroking hindwing by the synergic LEV–LEV interaction³⁷ with the shedding forewing upstroke LEV (LEV_{F1}) [see Figs. 7(c) and 13 (Multimedia view) $t/T = 4.1$ to 4.3]. Compared with the single hindwing case, this results in a lower pressure above the wing [Figs. 15(c) and 15(e) vs Figs. 15(d) and 15(f)] that explains the increased vertical force generation (reduced negative force).

Second, we can observe that the streamlines are strongly directed downward by the hindwing [Fig. 15(b)], very different from

the case seen in Fig. 14(b). It is evident that the drag as well as the lift in this case is higher as the momentum of the induced flow of the forewing is deflected more downward. The combined effect of these two flow features that occur briefly at the beginning of the upstroke results in the generation of a positive vertical force despite the upward motion of the hindwing but at the cost of inducing more drag (Fig. 14, $t/T = 4.3$).

In Figs. 16 and 17, the flow features during the down- and upstroke of the hindwing ($t/T = 4.1$ and 4.5) are shown in detail. Figures 16(a) and 17(a) show the iso-surfaces of Q-criterion in hindwing solo operation; furthermore, iso-surfaces of Q-criterion,

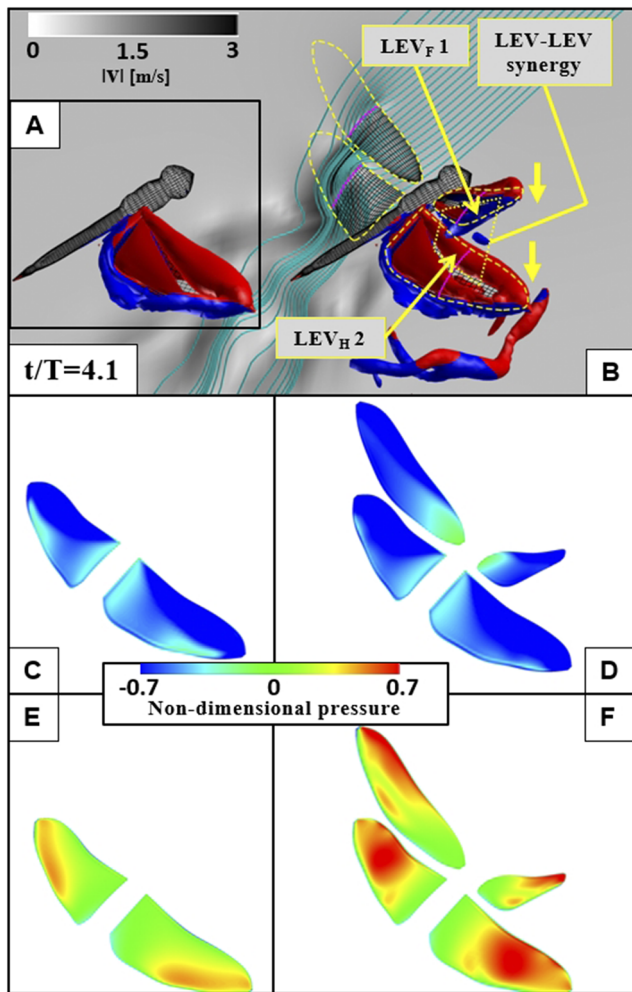


FIG. 16. (a) Iso-surfaces of Q-criterion ($Q = 1.2$ colored by Y-vorticity to indicate direction; red is positive and blue is negative), (b) iso-surfaces of $Q = 1.2$, streamlines and non-dimensional absolute velocity; and pressure distribution on the top [(c) and (d)] and bottom [(e) and (f)] wing surface at $t/T = 4.1$ in solo (a)–(c)–(e) and tandem (b)–(d)–(f) mode. The wings' motion is indicated by yellow arrows, and the midspan is highlighted by the pink line for reference. t/T is the dimensionless time, where T is the period and $t = 0$ at the start of the downstroke of the forewing in the first flapping cycle. lv is the velocity magnitude at the mid-span cross section.

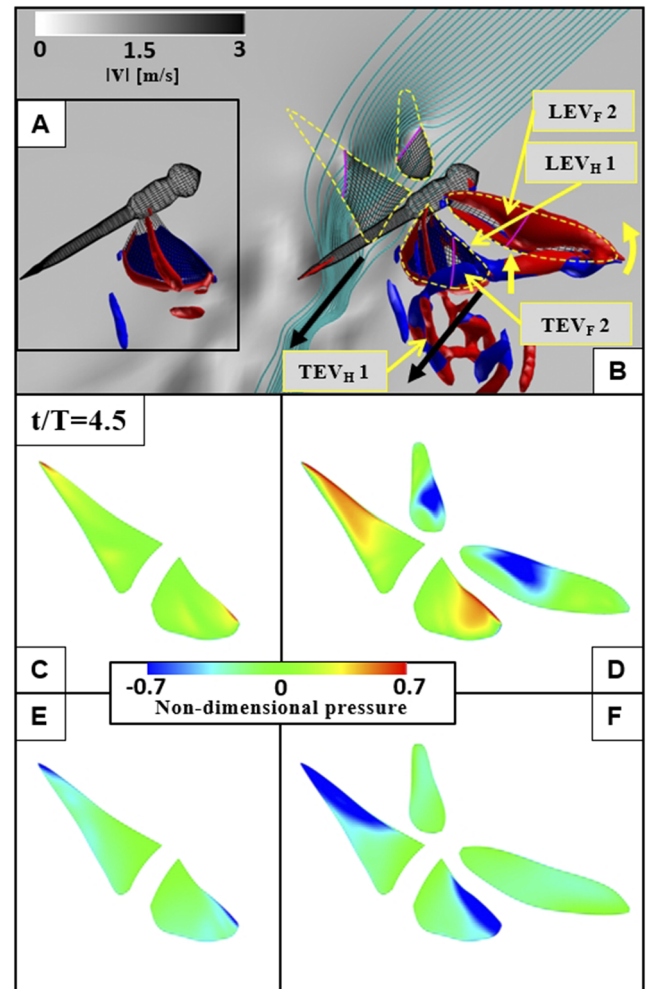


FIG. 17. (a) Iso-surface of Q-criterion ($Q = 1.2$ colored by Y-vorticity to indicate direction; red is positive and blue is negative), (b) iso-surfaces of $Q = 1.2$, streamlines and non-dimensional absolute velocity; and pressure distribution on the top [(c) and (d)] and bottom [(e) and (f)] wing surface at $t/T = 4.5$ in solo (a)–(c)–(e) and tandem (b)–(d)–(f) mode. The wings' motion is indicated by yellow arrows, and the midspan is highlighted by the pink line for reference. t/T is the dimensionless time, where T is the period and $t = 0$ at the start of the downstroke of the forewing in the first flapping cycle. lv is the velocity magnitude at the mid-span cross section.

velocity magnitude and streamlines at mid-span [Figs. 16(b) and 17(b)], are shown in tandem operation. We also present the non-dimensionalized pressure distribution on the wing surfaces in solo [Figs. 16(c), 16(e), 17(c), and 17(e)] and tandem [Figs. 16(d), 16(f), 17(d), and 17(f)] mode.

Figure 16 shows the hindwing in the final quarter of its downstroke. We can see that the forewing (LEV_{F1}) and hindwing (LEV_{H2}) LEVs are positioned close to each other [Fig. 16(b)]. The distance between the vortices facilitates a synergic interaction between these vortices.³⁷ In accordance with the flow structures, compared with the case of the single hindwing [Figs. 16(c)

and 16(e)], the surface pressure in the tandem mode [Figs. 16(d) and 16(f)] shows an area of higher pressure gradient between the bottom and top surface of the hindwing. This area spans from $0.3 S_{HW}$ to $0.8 S_{HW}$. This results in a force modulation that is shown in Fig. 12 ($t/T = 4.1$). There is neither a strong contraction nor a strong deflection of the streamlines in the mid-span cross section, which would foster increased horizontal momentum transport.

During the upstroke of the hindwing, according to the force graphs (Fig. 12), the interaction strongly affects the force generation over an extended area that is well indicated on the surface pressure plots in Fig. 17. Just after the mid-upstroke of the hindwing ($t/T = 4.5$), we can see a substantial difference in surface pressure distribution when comparing the solo vs the tandem operation of the hindwing [Figs. 17(c) and 17(e) vs Figs. 17(d) and 17(f)]. Study of the iso-surfaces of Q -criterion in relation to the wings' position and the streamline paths in Figs. 17(a) and 17(b) reveals three distinct features of the flow around the wings. The added effect of these features results in the particularly large aerodynamic force modulation. First, the synergic interaction with the forewing LEV (LEV_{F_2}) in the inner and mid-region of the hindwing boosts the upstroke hindwing LEV (LEV_{H_1}) and second, capture of the forewing wake vortex (TEV_{F_2}) in the tip region. And finally, we can observe that the shed hindwing (TEV_{H_1}) and forewing (TEV_{F_2}) vortices formed during the previous stroke create a narrow channel [shown by black arrow in Fig. 17(b)] in the wake of the wings that compress and direct the momentum of the induced flow resulting in propulsive output of the tandem wing system. This channel is not formed while the hindwing is downstroking [see streamlines in Fig. 17(b) vs

Fig. 16(b)], which also explains the remarkable difference in horizontal force modulation shown in Figs. 12(a) and 12(b) at t/T 4.1 vs t/T 4.5.

In Fig. 18, the modulation of the hindwing force generation during both downstroke and upstroke as well as over a complete flapping cycle is presented resolved to the wingspan. The interaction effect on the cycle-averaged vertical force generation of the hindwing is minimal, and it changes little over the span of the wing. Slightly larger modulation occurs in the midspan than at the root and the tip region of the wing. The cycle-averaged vertical force is decreased by the effect of the interaction over the complete span of the hindwing. During the downstroke of the hindwing, the vertical force modulation is in the outer span ($0.6 S_{HW}$ to $1 S_{HW}$) of the hindwing, while the modulation during the upstroke is in the region of $0.2 S_{HW}$ to $0.6 S_{HW}$. The outer span vertical force modulation is caused by the capture and interaction with shed vortical elements of the forewing (Figs. 14 and 16). The inner span vertical force modulation is the result of the hindwing's interaction with the forewing LEV.

The cycle-averaged horizontal force generation is increased over the complete span, most substantially in the midspan region (Fig. 18). During the downstroke, the horizontal force is decreased by the effect of the interaction; however, during upstroke, it is greatly increased. As shown by the numerical model [Figs. 15(b) and 17(b)], the horizontal force modulation is the combined result of the forewing LEVs synergic interaction with the hindwing LEVs and the wake vortex capture in addition to the momentum channeling of the wings' and wake vortices. In the body-fixed coordinate system, the interaction increases the horizontal force largely and most

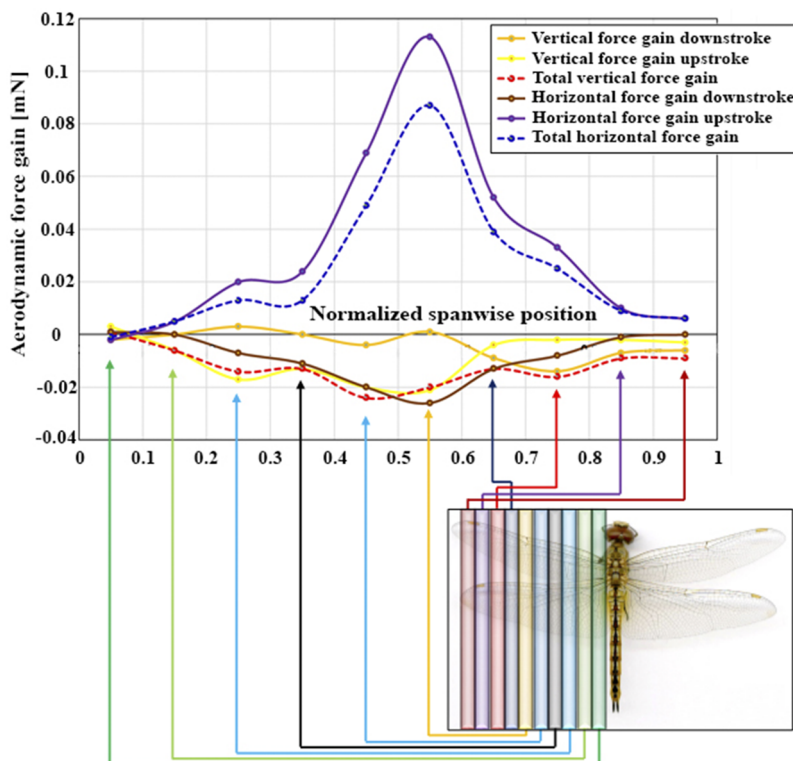


FIG. 18. Force gain of the hindwing by the interaction, resolved to the wingspan.

prominently in the midspan region while maintaining the vertical force. The increase in the horizontal force in the body-fixed reference frame contributes to thrust and weight support in the global coordinate system; thus, the interaction is advantageous in both thrust and lift generation.

IV. CONCLUSION

A comprehensive study has been conducted using experimental and numerical methodology to evaluate the aerodynamic characteristics of free-flying dragonflies, resolved along the wingspan. The numerical model is based on a high precision, dynamic wing-shape measurement of a free-flying dragonfly. The results of the numerical study show reasonable agreement with our earlier flow measurement on tethered specimens;³⁷ moreover, the interaction patterns closely match those measured on free-flying dragonflies. The numerical study thus serves as a tool for a span-resolved performance evaluation together with the time-resolved flow measurement. This integrated approach provides several results regarding the dragonflies' tandem wing operation:

- The flapping wings deform substantially. The chordwise cambering of the wings is related to the local chord length, while the twisting gradually increases toward the tip. Supported by the strong leading edge veins and corrugations, the spanwise cambering of the wings is not substantial. The flexible deformation of the wings helps preserve vortical structures on the wings' pressure side well after stroke reversal, which facilitates a LEV–LEV synergy and the shedding of consistent wake vortexes in the wake.
- Besides the downwash flow that is generally known to be present in the wake of the forewing, there are two distinct vortex interaction features that affect the hindwing. A synergic LEV–LEV interaction dominates the inner and mid-span regions, while a wake vortex capture is observed on the outer span.
- Evaluating the force generation on a systems level provides very little information. We can see that both wings generate most of the vertical force during downstroke and horizontal force during upstroke. The total vertical force is always positive, while the total thrust force oscillates with twice the flapping frequency. Only the hindwing generates substantial drag. Regarding the interaction effect on the hindwing, we can observe a time delay in both vertical and horizontal force building up during the downstroke, unlike during the upstroke. The peak forces are increased during both downstroke and upstroke. The largest modulation takes place during the upstroke when the horizontal force is boosted.
- Applying a span-resolved approach, we confirmed that the wings function differently over the span. The effect of the forewing–hindwing interaction on the horizontal force generation of the hindwing is largest at the midspan during both downstroke and upstroke. The vertical force modulation of the hindwing is small and decreases the lift. During the downstroke, it results from the interaction on the outer span, while during the upstroke, it results from the interaction in the inner span.

Regarding the cycle-averaged force modulation of the hindwing, the vertical force slightly decreases over the complete span with little variance. The largest modulation occurs at $0.4\text{--}0.5 S_{HW}$ and it decreases gradually toward the tip and the root. The horizontal force is increased considerably by the interaction, and the modulation is distributed around $0.5\text{--}0.6 S_{HW}$ with slightly larger modulation toward the tip. The increase in horizontal force generation is nearly equal to the decrease in vertical force generation in the inner $0\text{--}0.4 S_{HW}$ and the outermost $0.8\text{--}1 S_{HW}$. In the region of $0.4\text{--}0.8 S_{HW}$, the interaction increases the force generation because of the substantially larger horizontal force modulation that, in the global coordinate system, contributes to both lift and thrust generation.

Our results contribute to a better interpretation of the wing–wing interactions of a dragonfly with realistic wing shapes and detailed spatial–temporal characterization. We hope that these findings provide useful data and inspiration to artificial wing development for tandem winged MAVs.

ACKNOWLEDGMENTS

This research was supported by the Hong Kong Ph.D. Fellowship Scheme from the Research Grants Council (RGC), the Government of the Hong Kong Special Administrative Region (HKSAR), and the Hong Kong University of Science and Technology. The authors would also like to express their gratitude to Professor H. Liu from Chiba University for providing software and hardware resources for the numerical computations.

REFERENCES

- ¹W. Shyy, Y. Lian, J. Tang, D. Vîieru, and H. Liu, *Aerodynamics of Low Reynolds Number Flyers* (Cambridge University Press, New York, USA, 2008).
- ²W. Shyy, H. Aono, C.-K. Kang, and H. Liu, *An Introduction to Flapping Wing Aerodynamics* (Cambridge University Press, New York, USA, 2013).
- ³T. J. Mueller, *Fixed and Flapping Wing Aerodynamics for Micro Air Vehicle Applications* (American Institute of Aeronautics and Astronautics, Reston, VA, 2001).
- ⁴R. Å. Norberg, "Hovering flight of the dragonfly: *Aeschna Juncea* L., kinematics and aerodynamics," in *Swimming and Flying in Nature* (Springer, Boston, MA, 1975), Vol. 2, pp. 763–780.
- ⁵D. E. Alexander, "Unusual phase relationships between the forewings and hindwings in flying dragonflies," *J. Exp. Biol.* **109**, 379–383 (1984).
- ⁶G. Rüppell, "Kinematic analysis of symmetrical flight manoeuvres of odonata," *J. Exp. Biol.* **144**, 13–42 (1989).
- ⁷C. Soms and M. Luttges, "Dragonfly flight: Novel uses of unsteady separated flows," *Science* **228**, 1326–1329 (1985).
- ⁸M. A. Reavis and M. W. Luttges, "Aerodynamic forces produced by a dragonfly," *AIAA J.* **88**(0330), 1–13 (1988).
- ⁹F. O. Lehmann, "When wings touch wakes: Understanding locomotor force control by wake–wing interference in insect wings," *J. Exp. Biol.* **211**, 224–233 (2015).
- ¹⁰T. L. Hedrick, S. A. Combes, and L. A. Miller, "Recent developments in the study of insect flight," *Can. J. Zool.* **93**, 925–943 (2015).
- ¹¹D. D. Chin and D. Lentink, "Flapping wing aerodynamics: From insects to vertebrates," *J. Exp. Biol.* **219**, 920–932 (2016).
- ¹²S. Lan and M. Sun, "Aerodynamic force and flow structures of two airfoils in flapping motions," *Acta Mech. Sin.* **17**(4), 310–331 (2001).

- ¹³M. Sun and S. L. Lan, "A computational study of the aerodynamic forces and power requirements of dragonfly hovering," *J. Exp. Biol.* **207**, 1887–1901 (2004).
- ¹⁴Z. J. Wang and D. Russell, "Effect of forewing and hindwing interactions on aerodynamic forces and power in hovering dragonfly flight," *Phys. Rev. Lett.* **99**, 148101 (2007).
- ¹⁵K. Isogai, S. Fujishiro, T. Saitoh, M. Yamamoto, M. Yamasaki, and M. Matsubara, "Unsteady three-dimensional viscous flow simulation of a dragonfly hovering," *AIAA J.* **42**(10), 2053–2059 (2004).
- ¹⁶W. J. Maybury and F. O. Lehmann, "The fluid dynamics of flight control by kinematic phase lag variation between two robotic insect wings," *J. Exp. Biol.* **207**, 4707–4726 (2004).
- ¹⁷M. Yamamoto and K. Isogai, "Direct measurement of unsteady fluid dynamic forces for a hovering dragonfly," *AIAA J.* **43**(12), 2475–2480 (2005).
- ¹⁸J. R. Usherwood and F.-O. Lehmann, "Phasing of dragonfly wings can improve aerodynamic efficiency by removing swirl," *J. R. Soc., Interface* **5**(28), 1303–1307 (2008).
- ¹⁹D. Rival, D. Schönweitz, and C. Tropea, "Vortex interaction of tandem pitching and plunging plates: A two-dimensional model of hovering dragonfly-like flight," *Bioinspiration Biomimetics* **6**, 016008 (2011).
- ²⁰Z. Hu and X.-Y. Deng, "Aerodynamic interaction between forewing and hindwing of a hovering dragonfly," *Acta Mech. Sin.* **30**(6), 787–799 (2014).
- ²¹A. Azuma and T. Watanabe, "Flight performance of a dragonfly," *J. Exp. Biol.* **137**, 221–252 (1988).
- ²²J. M. Wakeling and C. P. Ellington, "Dragonfly Flight. II. Velocities, accelerations, and kinematics of flapping flight," *J. Exp. Biol.* **200**, 557–582 (1997).
- ²³M. H. Dickinson and K. G. Götz, "Unsteady aerodynamic performance of model wings at low Reynolds numbers," *J. Exp. Biol.* **174**, 45–64 (1993).
- ²⁴C. P. Ellington, C. Van den Berg, A. P. Willmott, and A. L. R. Thomas, "Leading-edge vortices in insect flight," *Nature* **384**, 626–630 (1996).
- ²⁵M. H. Dickinson, F. O. Lehmann, and S. P. Sane, "Wing rotation and the aerodynamic basis of insect flight," *Science* **284**(5422), 1954–1960 (1999).
- ²⁶S. P. Sane, "The aerodynamics of insect flight," *J. Exp. Biol.* **206**, 4191–4208 (2003).
- ²⁷J. M. Birch, W. B. Dickson, and M. H. Dickinson, "Force production and flow structure of the leading edge vortex on flapping wings at high and low Reynolds numbers," *J. Exp. Biol.* **207**, 1063–1072 (2004).
- ²⁸W. Shyy and H. Liu, "Flapping wings and aerodynamic lift: The role of leading-edge vortices," *AIAA J.* **45**(12), 2817–2819 (2007).
- ²⁹C.-M. Xie and W.-X. Huang, "Vortex interactions between forewing and hindwing of dragonfly in hovering flight," *Theor. Appl. Mech. Lett.* **5**, 24–29 (2015).
- ³⁰D. Rival, G. Hass, and C. Tropea, "Recovery of energy from leading- and trailing-edge vortices in tandem-airfoil configurations," *J. Aircr.* **48**, 203–211 (2011).
- ³¹T. M. Broering, Y. S. Lian, and W. Henshaw, "Numerical investigation of energy extraction in a tandem flapping wing configuration," *AIAA J.* **50**(11), 2295–2307 (2012).
- ³²Y. Zheng, Y. Wu, and H. Tang, "Force measurements of flexible tandem wings in hovering and forward flights," *Bioinspiration Biomimetics* **10**(1), 016021 (2015).
- ³³Y. Zheng, Y. Wu, and H. Tang, "An experimental study on the forewing-hindwing interactions in hovering and forward flights," *Int. J. Heat Fluid Flow* **59**, 62–73 (2016).
- ³⁴T. M. Broering and Y.-S. Lian, "The effect of phase angle and wing spacing on tandem flapping wings," *Acta Mech. Sin.* **28**, 1557–1571 (2012).
- ³⁵J. K. Wang and M. Sun, "A computational study of the aerodynamics and forewing-hindwing interaction of a model dragonfly in forward flight," *J. Exp. Biol.* **208**, 3785–3804 (2005).
- ³⁶H. Huang and M. Sun, "Dragonfly forewing-hindwing interaction at various flight speeds and wing phasing," *AIAA J.* **45**, 508–511 (2007).
- ³⁷C. Hefler, H. Qiu, and W. Shyy, "Aerodynamic characteristics along the wing span of a dragonfly *Pantala flavescens*," *J. Exp. Biol.* **221**, jeb171199 (2018).
- ³⁸A. L. R. Thomas, G. K. Taylor, R. B. Srygley, R. L. Nudds, and R. J. Bomphrey, "Dragonfly flight: Free-flight and tethered flow visualizations reveal a diverse array of unsteady lift-generating mechanisms, controlled primarily via angle of attack," *J. Exp. Biol.* **207**, 4299–4323 (2004).
- ³⁹R. J. Bomphrey, T. Nakata, P. Henningsson, and H.-T. Lin, "Flight of the dragonflies and damselflies," *Philos. Trans. R. Soc., B* **371**, 20150389 (2016).
- ⁴⁰M. Raffel, C. E. Willert, F. Scarano, C. J. Kahler, S. T. Wereley, and J. Kompenhans, *Particle Image Velocimetry—A Practical Guide*, 3rd ed. (Springer International Publishing AG, Cham, Switzerland, 2018).
- ⁴¹T. L. Hedrick, "Software techniques for two- and three-dimensional kinematic measurements of biological and biomimetic systems," *Bioinspiration Biomimetics* **3**, 034001 (2008).
- ⁴²H. Liu, "Integrated modeling of insect flight: From morphology, kinematics to aerodynamics," *J. Comput. Phys.* **228**, 439–459 (2009).
- ⁴³H. Liu and K. Kawachi, "A numerical study of insect flight," *J. Comput. Phys.* **146**, 124–156 (1998).
- ⁴⁴T. Nakata, H. Liu, Y. Tanaka, N. Nishihashi, X. Wang, and A. Sato, "Aerodynamics of a bio-inspired flexible flapping-wing micro air vehicle," *Bioinspiration Biomimetics* **6**, 045002 (2011).
- ⁴⁵A. Azuma, S. Azuma, I. Watanabe, and T. Furuta, "Flight mechanics of a dragonfly," *J. Exp. Biol.* **116**, 79–107 (1985).
- ⁴⁶N. M. Shumway, M. Gabryszak, and S. J. Laurence, "Flapping tandem-wing aerodynamics: Dragonflies in steady forward flight," in *AIAA Aerospace Sciences Meeting* (AIAA, Kissimmee, Florida, 2018).